Title	Simple characterization scheme for optical coherence tomography systems with application to a commercial and a near-isometric resolution fibre-based system
Author(s)	Dey, Rajib; Zhou, Yi; Neuhaus, Kai; Alexandrov, Sergey; Nolan, Andrew; Chang, Ting-Chiao; Leahy, Martin
Publication Date	2021-12-14
Publication Information	Dey, R., Zhou, Y., Neuhaus, K., Alexandrov, S., Nolan, A., Chang, T. C., & Leahy, M. (2022). Simple Characterization Scheme for Optical Coherence Tomography Systems With Application to a Commercial and a Near-Isometric Resolution Fibre-Based System. IEEE Photonics Journal, 14(1), 1-11. doi: 10.1109/JPHOT.2021.3135058
Link to publisher's version	https://dx.doi.org/10.1109/JPHOT.2021.3135058
Item record	http://hdl.handle.net/10379/17107
DOI	http://dx.doi.org/10.1109/JPHOT.2021.3135058

Simple Characterization Scheme for Optical Coherence Tomography Systems With Application to a Commercial and a Near-Isometric Resolution Fibre-Based System

Rajib Dey , Yi Zhou, Kai Neuhaus , *Member, IEEE*, Sergey Alexandrov , Andrew Nolan, Ting-Chiao Chang, and Martin Leahy

Abstract—Optical Coherence Tomography (OCT) is a rapidly growing imaging modality in biomedical optics. OCT can perform high-resolution, cross-sectional imaging of the microstructure of biological tissues by measuring the coherent spectrum from the backscattered light. OCT systems with broad spectral bandwidths are often constructed using free-space optics to avoid dispersion by fibre optic components. This paper presents a fibre-based OCT system at a centre wavelength of 1300 nm with an axial resolution of 3.8 μm in air, surpassing any previously reported values to the best of our knowledge. Despite the challenges in transporting a broadband spectrum using fibre-optics, the system investigation was motivated by the ever-increasing demand for commercialization of high-resolution OCT systems and simplification of construction. We also evaluate and demonstrate the direct measurement method for axial resolution using an air wedge. Imaging of biomedical and other samples is demonstrated using a high numerical aperture sample lens and compared with images from a commercial OCT system. We discuss the effect of the improved structural visibility by achieving image voxels closer to an isometric shape with a high NA sample lens.

Index Terms—Optical coherence tomography, supercontinuum generation, high-resolution imaging, spatial resolution, image analysis, image quality, isometric resolution.

I. INTRODUCTION

OPTICAL coherence tomography (OCT) is a high speed, noncontact, non-invasive imaging technology that provides high axial resolution to depths of 1 to 2 millimetres within biological samples [1], [2]. OCT is a powerful imaging technique which facilitates depth resolved information from interferometrically separated backscattered photons from different layers of samples. OCT is widely used for both structural and functional imaging applications for disease diagnosis such as that of the eye [3], [4], heart and blood vessels [5]–[8], tumours [9], [10], visualization of dental structure [11]–[13], diagnosis and treatment of skin disorders [14]–[16]. OCT is used for imaging in material science [17], structural analysis of polymer composites [18], [19], sensor technology [20], [21], among many other applications. Spectral-domain OCT (SD-OCT) is a widely used modality due to its high sensitivity and fast imaging speed [22]–[26].

The axial resolution of OCT is inversely proportional to the bandwidth and proportional to the central wavelength of the light source [27]. With the development of high-resolution spectral-domain OCT (HR-SD-OCT), supercontinuum generation light sources have attracted much attention in the last two decades. Supercontinuum generation light sources have several advantages over super luminescent diodes such as high output power, extremely broad spectral bandwidths, and a high degree of spatial coherence. M. Szkulmowski *et al.* first demonstrated a free space spectral domain OCT system with a supercontinuum light source for high resolution in vivo imaging, and achieved 4 μm axial OCT image resolution and 20 μm lateral resolution in the 0.75 μm to 0.95 μm spectral window [28]. Suitable spectral bandwidth for deep imaging in tissue is around of 1300 nm P. Cimalla *et al.* demonstrated a dual-band, free space SD-OCT system based on a supercontinuum laser. They reported 4.5 μm and 7 μm axial resolution in air within the spectral windows of 0.7 μm to 0.9 μm and 1.1 μm to 1.4 μm, respectively [29]. These proposed supercontinuum SD-OCT systems were mainly based on free-space optics. Several OCT research groups have developed free-space TD-OCT and SD-OCT [6], [30] systems using supercontinuum light sources but only a few research groups have demonstrated supercontinuum source and fibre-based SD-OCT systems (Table I) centred at 1300 nm wavelength corresponding to an axial and lateral resolution of 8 μm and 15 μm in air [31], [32]. M. Maria *et al.* compared the noise performance of three different supercontinuum light sources using a fibre-based OCT configuration [33]. Although, it is to be expected that the axial resolution may improve with increased

TABLE I
PUBLIC REPORTED AXIAL RESOLUTION OF FIBRE-OPTIC BASED HR-SD-OCT
SYSTEMS WITH CENTRE WAVELENGTH OF 1300 nm

| Authors	Axial resolution (μm)	Lateral resolution (μm)
Yi-Jing You, et al., Laser Phys. Lett., 2015 [31].	8.1 (air)	Not stated.
C. Chen, et al., Biomed. Opt. Express., 2018 [32].	8 (air)	15
M. Maria et al., Proc. Of SPIE, 2017 [33].	4 (air)	Not stated.
Presented System	3.8 (air)	5.5

Fig. 1. Schematic of fibre-based high resolution spectral domain OCT system. SC Laser: Supercontinuum laser source, SuperK splitter, Long pass, short pass and neutral density filters, OC: Optical Circulator, FC: 2×2 fibre coupler. L: Lenses, L5: Objective lens, RM: Reference mirror, X-Y Galvo, DG: Diffraction Grating.

spectral bandwidth, we discuss the air-wedge method for direct evaluation of the axial resolution. Also, more accurate characterization may become more relevant for fibre-based OCT systems in the future, to provide improved tuning and calibration. Moreover, our system design evaluates the use of a high NA sample lens to improve isometry of the image voxel, which becomes relevant with improved axial resolution. Although many system designs try to maximize imaging depth using lower NA sample lenses, high NA sample lenses are of interest for improved sensitivity to small structures in shallower sample regions, such as for skin cancer detection. K. C. Zhou *et al.* and C. K. Chang *et al.* have discussed the importance of isometric resolution in OCT [34]–[36].

As the system designed for this study is intended for skin imaging, a centre wavelength at 1300 nm was chosen because it offers the best compromise between penetration depth, water absorption, and axial resolution. In biological applications, scattering and water absorption are highly dependent on the wavelength of the light source. In the longer wavelength region, it can enhance penetration depth and imaging contrast due to low scattering at deeper penetration depths where multiple scattered photons dominate over ballistic photons [37], [38], and absorption will be reasonably low.

A fibre-based SD-OCT system has advantages over free space regarding commercialized designs. fibre-optics are easier to assemble, have better stability (less sensitive to vibration, airflow, and temperature fluctuation), and handling is simplified, which may be important for the construction of future medical imaging devices. In this paper, we present a high axial resolution of 3.7 μm based on the bandwidth of the light-source and a measured resolution in air of 3.8 μm. We experimentally validate a lateral resolution of 5.5 μm using a USAF target with a fibre-based HR-SD-OCT system with a supercontinuum light source and a spectral window between 1100 nm to 1500 nm. We also provide a more rigorous analysis using an air-wedge for the characterization and validation of the axial resolution. The maximum sensitivity was measured to be 109 dB at an A-line rate of 73 kHz averaging 1024 A-lines. We demonstrate imaging on biological tissue, including qualitative discussion.

Along with the OCT system characterization, we evaluate a low-cost air-wedge-based measurement standard. Many publications suggest a wide variety of OCT phantoms that are often difficult to replicate or impossible to obtain commercially. For instance, the APL-OP01 OCT phantom (Arden photonics Ltd.)
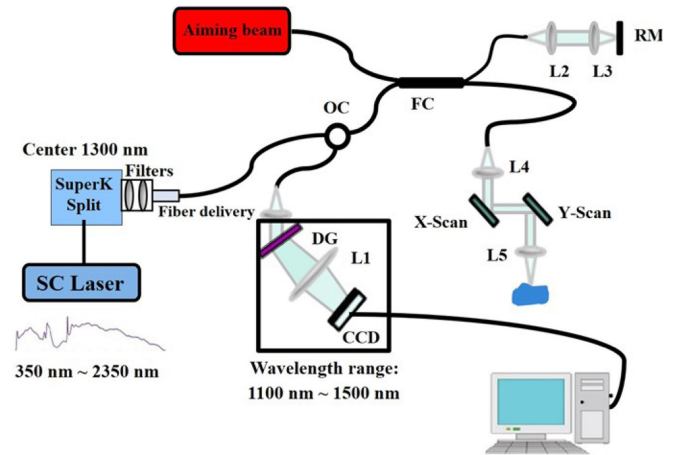
is a valuable and easily applicable standard that characterizes essential parameters for OCT systems. Whereas the commercial phantom provides good repeatability of geometric structures and allows characterizing the PSF on inscribed reflectors and different depth positions, it would not allow direct measurement of the axial resolution limits as it would be difficult to provide embedded reflecting structures with known size and sufficient accuracy. Laser inscription of structures into fused silica is a favoured method in laboratories that have suitable laser equipment and expertise to create phantoms with known structures [39]. Also, the air wedge using standard microscope slides will not be able to provide high accuracy. However, a user or a well-equipped laboratory may find it easy to modify the construction with more accurate methods and materials, offering the flexibility to design a phantom for specific characterization goals. For instance, different wedge slopes may be of interest in studying the impact of interference artefacts on closely spaced structures and layers. Moreover, the wedge can be embedded in different liquids to study different effects due to refractive index changes and dispersion still having the capability to modify the wedge spacing.

II. SYSTEM DESIGN AND MEASUREMENTS

A. System Setup

For this study, no detailed evaluation of the relative intensity noise (RIN) was performed, as it would not contribute significantly to the evaluation of the axial resolution. The supercontinuum light source (SuperK EXU6, NKT Photonics) is advertised for OCT applications, suggesting that the RIN values are better than 100 dB.

Our system design (see schematic Fig. 1) uses a low noise, non-polarized, supercontinuum light source (SuperK EXU6, NKT Photonics) with a central wavelength of 1300 nm (SC Laser). The bandwidth of the light source spectrum was reduced

to about 400 nm using a short pass filter (Edmund optics, SN: 84656, OD2, wavelength range: 810–2025 nm, transmission wavelength: 810–1540 nm, rejection wavelength: 1700–2025 nm) and long pass filter (Semrock, SN: BLP01-1064R-25, transmission band: 1093.8–1600 nm). The output power is attenuated using an optical splitter (SuperK connect, NKT Photonics, wavelength range 400–2000 nm). A broadband fibre delivery system (SuperK FD5 non-PM, NKT Photonics, wavelength range 950–1530 nm) is used to inject the light source into the Michelson interferometer (MI). To avoid back propagation of light to the light source, an optical circulator is used (Precision Micro-Optics, 1310 nm SM Circulator, SN: 2017123002).

The MI is constructed using a 90/10 beam splitter (Thorlabs, SN: T030932, 2×2 90:10 wideband coupler) providing 90 percent sample arm power and 10 percent reference arm power (FC). For the sample arm fibre, a collimator (L4) with a focal length $f = 11$ mm is used (Thorlabs, Inc., Part No. F280APC-C) projecting the beam onto an X-Y galvanometer (Thorlabs, Part No. GVS112). The sample objective lens (L5) is an M Plan Apo with $10\times$ magnification, NA $= 0.26$, and $f = 20$ mm. For the reference arm, another collimator (L2) of the same type is used. The reference mirror (RM) is gold coated (Thorlabs, SN: ME1-M01) and for focusing, an achromatic doublet (Thorlabs, Achromatic Doublet, $f = 19$ mm) is used. For dispersion compensation, a 2 mm thick optical window between L2 and L3 is used (not shown in schematic). Tuning the dispersion compensation was performed by successively changing the path delay in the reference arm using different optical thicknesses while measuring the point-spread function. The output port of the circulator (OC) is connected to the spectrometer (Wasatch Photonics, Cobra 1300). The high-speed camera (CCD) is connected to the CameraLink frame grabber (Teledyne Dalsa, X64 Xcelera-CL PX4 Dual) and triggered by a digital input/output board. For lateral scanning, a two-axis galvo scanning system (Thorlabs, GVS112) is connected to a PCIe 6321 multifunctional I/O device (National Instrument, PCIe 6321). We developed custom software in Lab-VIEW for hardware control and data acquisition. Although for visualization, some pre-processing was performed in LabVIEW, signal and image processing of the raw data was performed in MATLAB. Signal and image processing steps included k-space linearization, spectral windowing (Hann), inverse Fast-Fourier Transform, and intensity log-scaling for display. The Hann window was selected due to its minimal spectral leakage and the optimal reproduction of the PSF [40].

B. Air Wedge Theory and Construction

The in-air axial resolution of OCT systems is conventionally provided based on the bandwidth of the used light source, and the point spread function (PSF) can be measured based on a mirror reflection in the sample arm of the Michelson interferometer. Some research groups are using beads embedded in a semi-transparent medium to demonstrate sensitivity and resolution, but preparation and lifetime limits access and usability. For lens based optical systems such as microscopes and telescopes the resolution limit is defined based on certain criteria, such as the better-known Rayleigh criterion, but also the Sparrow, Ricker,
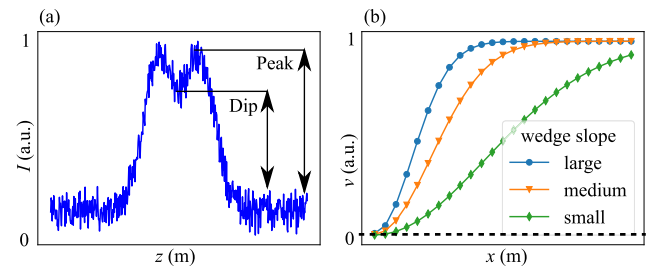

Fig. 2. Plot (a) shows the numerical simulation based on (2) of a noisy double peak with a visible dip with arbitrary intensity values I along depth z. Plot (b) shows the simulated noiseless visibility v ($v = p - d$; p ...peak height, d ...dip height) for two peaks originating from a wedge reflection that move closer together along a lateral position x. The true size of depth z and x will be in the millimetre range and is not to scale for illustrative purpose. Best visibility would be achieved at $d = 0$ and $p = 1$ corresponding to a peak of unity intensity. The three different plots relate to different wedge slopes or wedge spacing. The "narrow" curve relates to a thin spacing or shallow slope, "medium" some spacing between narrow and wide, and "wide" is the largest spacing or slope. The peaks would be fully merged at $x = 0$ (left) corresponding to the touching end of the wedge and fully separated for x position to the right. The ideal visibility starts to drop if the peak distance becomes smaller than the peak width. Without noise, the ideal visibility can be computed up to zero value.

Dawes's criterion, and most importantly the Abbé diffraction limit [41]–[46]. All criteria describe the resolution limit based on the separation of two PSF's that are mathematically described by the Airy function. The Airy function can be approximated with a Gaussian, which allows the measurement of the axial PSF of OCT systems with a Gaussian light source and using two reflecting surfaces or layers in the sample arm of the system's interferometer.

Although the theory of measuring the optical resolution and image quality is well understood, the process to perform accurate measurements requires suitable equipment depending on precision and accuracy required. This is especially true for OCT if one tries to plan for a suitable reflection standard that can generate two axial PSF's with sufficient accuracy. Nevertheless, we show that the noise is a major factor which limits measurement accuracy and a low-cost optical air-wedge may be sufficient for general characterization of the axial resolution of an OCT system.

We designed therefore a low-cost method to measure the axial resolution of OCT systems using a simple air wedge made of two microscope slides, Scotch tape and aluminium tape (Section III-B, Fig. 8). The air wedge is then moved along its length L and imaged multiple times at a position x depending on the scan range of the used OCT system. Although a translational stage can provide better positioning accuracy, price and size may not be suitable for all systems and would not help to get a continuous wedge image. We therefore designed suitable software that can process, align and position the imaged segments relative to each other based on the visible wedge spacing.

The dimensions of the wedge were measured using a micrometer screw gauge and calipers. Although air wedge interference can be used to characterize the wedge geometry to nanometre accuracy, the expected uncertainties of the wedge imaging would not benefit from it. Also, the expected fringe separation for the required wedge geometries based on Table II would be less
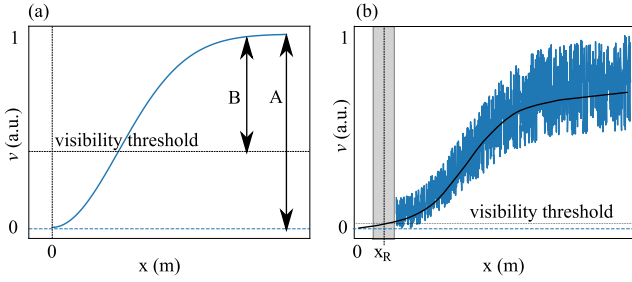
Fig. 3. (a) Shows the visibility function v for fitting with a visibility threshold due to parameter B related to (2). (b) Shows the visibility function v with added noise. Plots (a) and (b) use arbitrary lateral dimensional scale in meters which in practice will be in the millimetre range. The average visibility of a structure must be at least above some noise threshold, which relates to the visibility threshold indicated. The grey shaded range is where the fitted function (black) would predict zero visibility without noise. The zero visibility must occur at lateral position $x_R > 0$. Based on the lateral position x_R, the axial resolution d can be calculated using (2). The measured visibility in Section III-B confirms that the uncertainty impedes the detection of the peaks from the wedge reflections and the signal is lost before the lateral position $x = 0$ (Fig. 8).
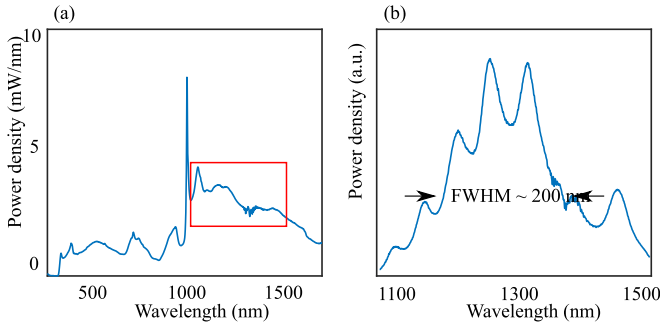

Fig. 4. Output spectra of the SuperK EXU6 laser source. The selected spectral window used is from 1100 to 1500 nm (red box). (b) Sample arm spectrum obtained from mirror reflection.

TABLE II
WE USED WEDGES WITH DIFFERENT SPACER THICKNESS TO EVALUATE THE
IMPACT OF THE WEDGE SLOPE ON THE GAP VISIBILITY

	Visible wedge length L (mm)	Spacer D (mm)
Wedge 1	71.0 ± 0.2	0.070 ± 0.006
Wedge 2	69.7 ± 0.2	0.123 ± 0.007
Wedge 3	67.4 ± 0.2	0.237 ± 0.005

than 280 microns and difficult to record accurately. The visible wedge length was measured with calipers to an uncertainty of 200 microns. Also, it could be argued that better accuracy could be achieved with a micrometer stage and microscope. The maximum error expected would be 0.7 μm based on the relation $x/d = L/D$ with x for any lateral position, d the wedge spacing at position x, L the visible wedge length, and D the spacer thickness. This 0.7 μm accuracy is far beyond the achievable imaging accuracy due to the additional uncertainties introduced by the image noise.

The noise of the image acquisition makes the largest contribution to the uncertainty, which is described in more detail, exploring the measurement theory. Although additional image averaging can reduce the noise further, it was of interest for this study to include the noise characteristics for comparison. On the

other hand, signal or image averaging may otherwise obfuscate artefacts, i.e., automatic adaptive contrast adjustments. The theory is based on the detection of the peak separation. As shown in Fig. 2, the visibility, v, can be defined by using the height of the peak, p, vs dip amplitude, d. The visibility, v, can then be described by the difference between the peak and dip height and plotted for a sequence of peak distances along a wedge position, x, including a peak standard deviation, σ (Fig. 2) corresponding to a peak width. The visibility, v, then follows the equation:

$$v = 1 - e^{-\frac{x^2}{\sigma^2}}. \tag{1}$$

Equation (1) only considers a noise-less signal, meaning a visibility up to a lateral zero position ($x = 0$) can be found corresponding to the thin end of wedge. However, measurements in Section III-B show that the visibility is lost before the lateral position of the touching ends of the wedge are reached ($x > 0$). It should be noted that we acknowledge that the image intensities and noise intensities are log scaled and that the linear difference is log scaled. However, as we consider the visibility as the difference between peak intensity of the wedge edges vs the intensity of the dip, the visibility has the relation as described by (2) and additional log scaling would not essentially improve details of the visibility measurements.

It is apparent from Fig. 2(a) that noise can obfuscate the dip, and the separation of two peaks cannot be determined if noise levels are too large. We can accommodate noise by adding the parameters for amplitude, A, and an uncertainty factor, B, to (1):

$$v = BA - Ae^{-\frac{x^2}{\sigma^2}}. \tag{2}$$

Equation (2) accommodates now the amplitude parameter, A, for normalizing visibility values or to fit against measurement data. The uncertainty factor, B, allows the shifting of the visibility curve in Fig. 3(b) such that negative visibilities can be computed that represent data that are not measurable due to noise. Please note that the effect of the uncertainty factor, B, is not noise and only accounts for the signal cut-off due to noise as shown in Fig. 3.

Uncertainty factor, B, forces the visibility amplitude, A, to be shifted such that some components have negative values that are not available as a signal. Fig. 3(b) shows the visibility computed using (2) and added variations, whereas values for visibility less than zero have been removed. Compared to the measured visibilities as shown in Section III-B, the modelled visibility (Fig. 3(b)) agrees well with the observed visibility characteristics.

The uncertainties of the visibility and B are difficult to measure accurately as they depend on many different factors that are not easy to control. For instance, the more obvious variations in the OCT reference system (Telesto III) are related to adaptive contrast optimization that becomes visible in the jagged uncertainty of the visibility (see figures in Section III-B). For the HR-SD-OCT system described in this manuscript, the high NA lens causes the uncertainty of visibility to change strongly over the scan range, which is clearly visible by the arc shaped characteristics in (see Section III-B). However, some upper
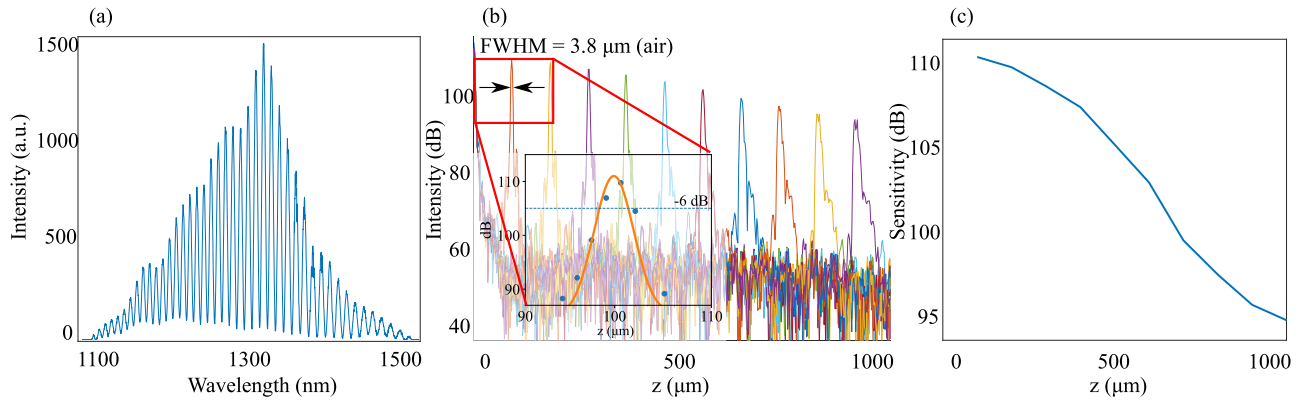
Fig. 5. (a) Interference pattern from sample mirror. (b) Measured axial PSF and roll-off over depth (z) and intensity in dB. The inset (red box) shows width of PSF at -6 dB from maximum at 100 μm depth. (c) Roll-off of sensitivity over a range of 1000 μm axial depth range.
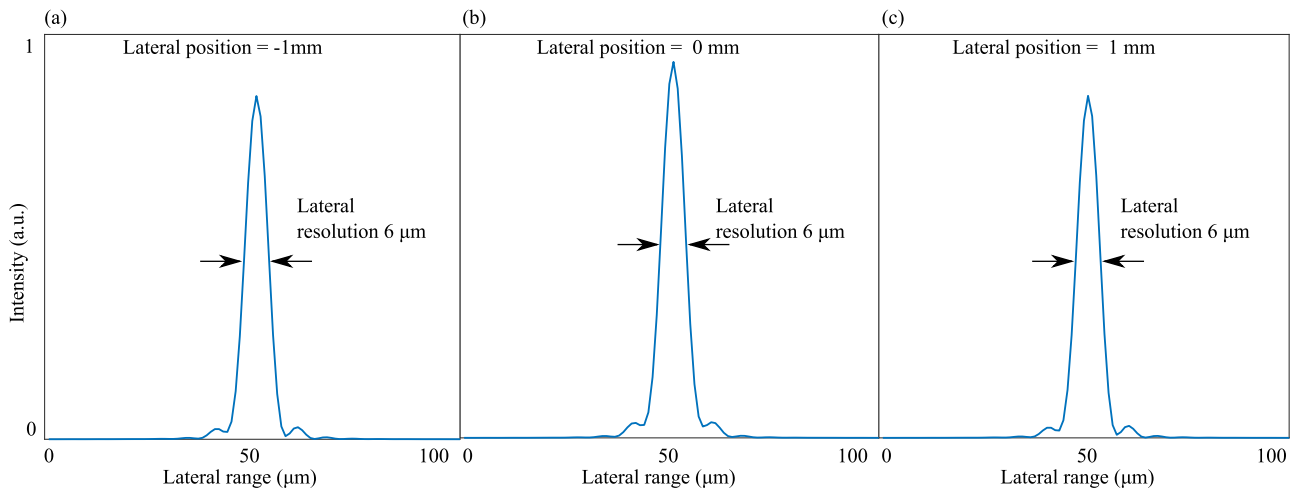

Fig. 6. The lateral PSF was simulated, using Zemax, for three lateral positions over a scan range of ± 1 mm from the principle axis. The simulation results show that the lateral PSF remains constant over the full scan range.
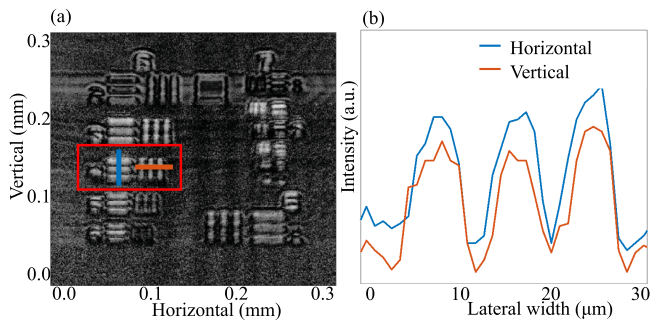

Fig. 7. Lateral resolution validation using USAF test target. (a) Zoomed in view of group 6 and 7 elements from Thorlabs (USAF1951). The last resolved line group is 6-4, highlighted in red colour box. (b) The line profile extracted from B-scan image across the vertical and horizontal direction of group 6-4.

and lower boundaries can be estimated based on the observed uncertainty and fitting with (2). Since (2) describes the ideal visibility without uncertainties from noise sources for $B = 1$, the curve trajectory would reach $x = 0$ and we can determine the theoretical wedge spacing $d = 0$ mm ($d = xL/D$). The lower boundary for the uncertainty factor must have a value $B < 1$. Based on the theory described and Fig. 3, the uncertainties in visibility show a clear cut-off along the lateral wedge position which can be used to estimate a value for B. Therefore, the fitting was performed for $B = 0.9$, 0.94, and 0.98. This allows the visibility to be followed close to the lowest uncertainties observed ($B = 0.90$), including fitting to the mean levels ($B = 0.98$). It should be noted that the if B is allowed to vary for fitting, the fitting algorithm does not converge or produces spurious visibility values larger than zero for the touching end.

III. MEASUREMENTS AND IMAGING RESULTS

A. Measured System Parameters

After power attenuation and spectral filtering, the sample arm power was measured to be 8 mW. Fig. 4(a) shows the spectrum of the laser source and the red box shows the selected spectral window. The optical components and optical fibre reshape the light source spectrum, and Fig. 4(b) shows the spectrum obtained
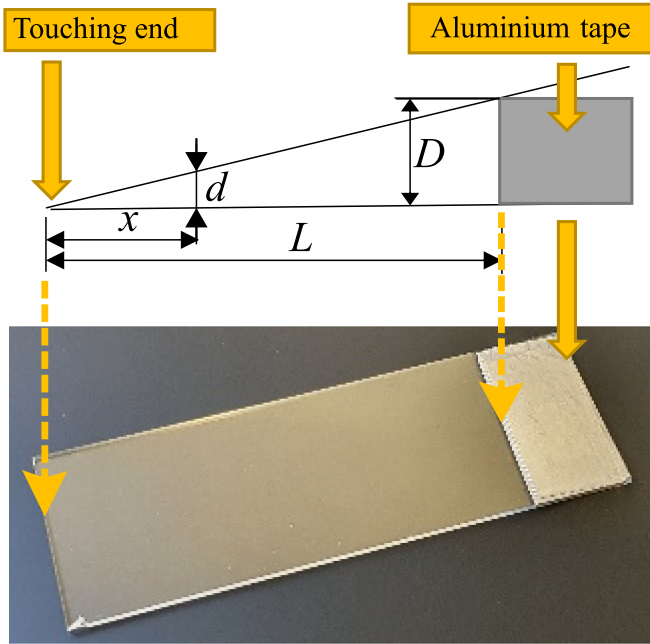
Fig. 8. The air-wedge geometry (top) related to the physical constructed wedge made of microscope slides (bottom). The geometry of the air-wedge is described by the visible length, L, the wedge spacer thickness, D, the lateral position, x, and the wedge gap, d, at this lateral position. The wedge gap, d, is assumed to be zero at the touching end. The average measured dimensions of the microscope slides are $L = (71.0, 69.7, 67.4)$ mm, $D = (0.070, 0.123, 0.237)$ mm (see Table II). The value x is measured by fitting in Fig. 9 and d is calculated with $d/x = D/L$.

from the sample mirror reflection. The spectrum ranges from 1100 to 1500 nm, is centred at around 1300 nm, and the full width at half maximum (FWHM) is about 200 nm. Fig. 5(a) shows an interference spectrum obtained from the HR-SD-OCT system. The axial resolution is defined as the FWHM of the coherence envelope of the interferogram, obtained by inverse Fourier transform. The PSF was measured from a sample mirror reflection at a depth of 100 μm in air and the best fit with a Gaussian provided a value of 3.8 μm as shown in Fig. 5(b). This measured axial PSF on a sample mirror agrees well with the calculated theoretical axial resolution value of 3.7 μm. Fig. 5(c) shows sensitivity roll-off from 109 to about 94 dB over a depth range of about 1 mm. The signal-to-noise ratio (SNR) of the system was measured as the difference between maximum peak amplitude and median of the noise floor of the depth profile of the dB scaled values. An SNR of 69 dB was measured using an OD2 optical attenuation (40 dB) in the sample arm with 1024 A-line averaging at the line rate of 73 kHz.

The properties of the high-NA lens were simulated with Zemax regarding the lateral PSF in air. Using the paraxial beam approximation and diffraction limited focal spot size at the focal plane, the pupil diameter was varied to find the optimal NA. It was found that an NA of 0.085 for an entrance pupil diameter of 3.4 mm provides an lateral PSF of 6.0 μm. The theoretical lateral resolution of 5.6 μm using $0.37 \cdot \lambda_0/\text{NA}$ agrees well with the simulated value. Fig. 6(a), (b), and (c) shows that the lateral

resolution of about 6 μm remains constant over a scan range of about 2 mm.

To verify the lateral resolution, an element group of an USAF test target was scanned with a focused beam and imaged. The en face image in Fig. 7(a) shows the 4th element of group 6, with line spacings of 11 microns. The width of a single element of 5.5 microns agrees well with the simulated lateral PSF in Fig. 6.

B. Air Wedge Measurement Methods and Results

Three different air-wedges were constructed (Fig. 8) from commercial microscope slides (VWR International, Cat. No. 631-0109) with dimensions of $(75 \times 26 \times 1)$ mm and spacer material of commercially available aluminium tape (Radionics, 3 M T117).

Three spacer thicknesses were used (Table II) to estimate the effect of noise, but also to obtain an estimate of measurement variance. The measurement uncertainties for the visible wedge lengths were chosen from the overall largest measured standard variation, assuming that smaller uncertainty values are coincidental. For the spacer thickness, the uncertainties are based on the standard deviation from at least six different measurements with the micrometer screw gauge.

The tape layers were applied on top of the carrier microscope slide and the total thickness was measured with a micrometer screw gauge (reading accuracy of 0.01 mm). Six or more readings were performed over multiple locations over the tape layers, and reading values between the ticks were added as estimates for the calculation of the standard deviation. It was found that the total thickness was constant, or any variations were beyond measurable. It should be noted that the total thickness of the tape layers is somewhat less compared to the suppliers' specifications due to the glue layer viscosity. The visible wedge length was then measured using a caliper.

To measure the visibility of the edges of the air-wedge, multiple image segments needed to be acquired over the visible wedge length. The described high-resolution OCT system is limited to a maximum scan range of 2.2 mm. Consequently, to cover a full wedge length, multiple image segments were acquired. The image segments were stored in separate image files and then processed and plotted (Fig. 9). For image processing, we used edge detection from scikit-image [47] and the LMFIT [48] package for curve fitting. The edge detection was used to allocate the wedge edges in the images corresponding to the peaks per A-line. Based on the edge location data, the segments were laterally aligned, and the peak and dip heights were measured in the original image. The difference of the peak and median dip height was collected to create the plots in Fig. 9.

The wedge imaging was performed to characterize the high-resolution system and compared to the images from a Telesto III (Thorlabs, Inc.) with a centre wavelength of 1300 nm, bandwidth larger than 170 nm, and 5.5 μm axial resolution in air. Fig. 9(a–c) shows the results for the Telesto III, Fig. 9(d–f) shows results for the described HR-SD-OCT system. Each column in Fig. 9 corresponds to a different wedge spacer thickness, as tabulated in Table II.
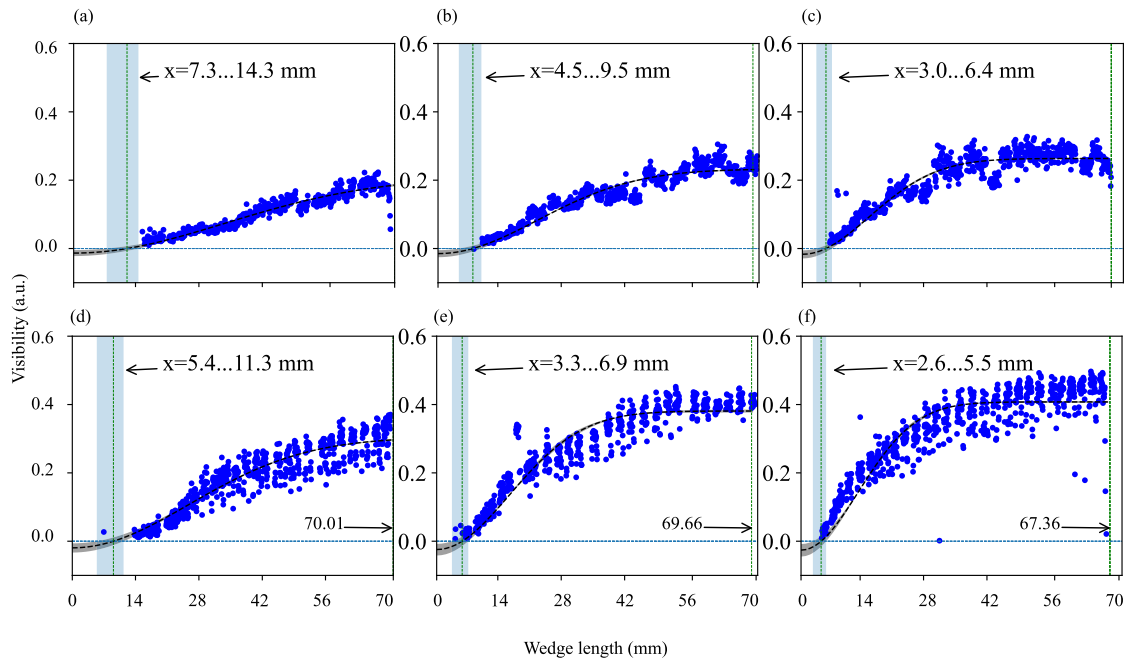
Fig. 9. Visibility measurements of Telesto III (a, b, c) and the high-resolution fibre optical OCT system (d, e, f). The fitting variance for the lateral position where visibility of the air gap is lost (for the factor $B = 0.90 \ldots 0.98$) is shown as grey shade and the black dash line is $B = 0.94$. The grey regions are the lateral wedge positions where potentially the wedge may still be visible. The edge detection does not detect peaks for the full visibility range, and the uncertainty of visibility increases. Nevertheless, wedge separation may still be detectable within this region and the fitting provides a valid extension of the missing data points. The jagged visibility characteristic for the Telesto III system originates most likely from automatic contrast optimization. The visibility plots were assembled from multiple small segments using a scan range of 2.2 mm to cover the full wedge length. The arc shaped segments for the described high-resolution OCT system originate from the high NA lens.

The results in Fig. 9 show how the visibility (blue) can be approximated using a model fit to find the actual smallest wedge space detectable. The model fit accounts for noise or the uncertainty of visibility using an uncertainty factor that is visible as the grey shaded range around the fitted curve. The uncertainty of visibility translates to an uncertainty laterally where the smallest wedge spacing can be predicted, shown as a vertical region in grey. The x values in the plot give the numeric range of the predicted lateral positions. Using the values for the wedge spacer given in Table II, the wedge spacing can be calculated using the simple relation $d/x = D/L$ as describe above. The value ranges for d are plotted in Fig. 10 showing the best estimates for the detection of wedge gaps.

It should be noted that ideally, the values for different wedge sizes should produce the same detectable wedge gap. However, it is to be expected that the noise for larger wedge slopes increases more rapidly if the wedge edges converge, which could be attributed to interference effects. Like the air-wedge interference visible with a sodium lamp, interference will occur in the OCT images as well [49]. We did not provide any images of such wedge interference as it was not very pronounced or visible as expected for light sources with a broader spectrum.

The investigation using simple microscope slides was motivated to understand the limitations of using a low-cost in-house construction method. The results show that the high reflectivity due to the air-glass interfaces causes camera saturation, and additional attenuation increases noise and reduces the visibility of smaller wedge spacings. A follow-up study could use
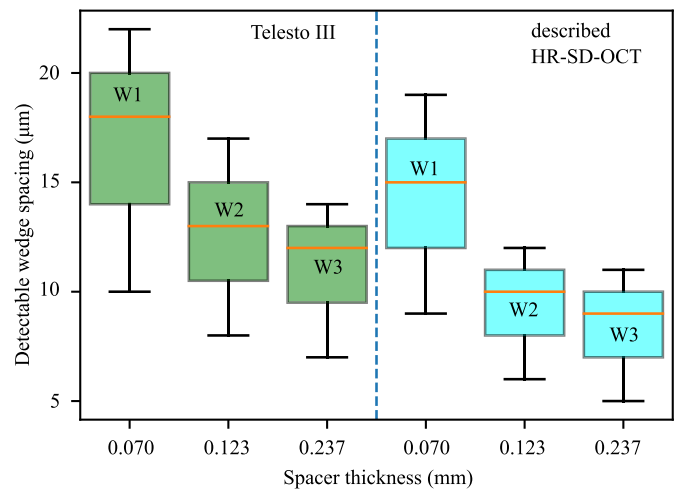

Fig. 10. Best detectable wedge spacings compared between Telesto III and the high-resolution system described. The mean difference between both systems is 2.8 microns, and the predicted improvement based on the light source bandwidth is 1.7 microns. Although the values fall within the uncertainties, the consistent difference for three different wedges provides some confidence in an actual resolution difference. The box plot centre values represent the median, the upper and lower box boundaries represent the first and third quartile. The whiskers extend 1.5 times from the upper and lower box boundaries representing the interquartile range giving some estimate of the distribution of data points.

commercial anti-reflective coated materials to investigate material properties most suitable for higher accuracy wedges. The

touching end of the microscope slides is considered the ground truth of a zero spacing that can never be imaged in practice. Only fitting a visibility model over measured wedge data allows estimating the lateral position x_R where the noiseless wedge visibility is lost. The calculation of the wedge spacing d at x_R is obtained from the relation $d/x_R = D/L$. Notably, any uncertainties and systematic errors of measuring D and L will cause increased uncertainty in the value d or even cause an offset deviating from the expected theoretical point-spread function. The uncertainties in x_R originate from the wedge visibility and fitting accuracy. The measured best resolution using the wedge in Fig. 10 is indeed much larger with around 8 microns compared to the expected axial resolution of 3.8 microns measured on a single A-line profile (Fig. 5). Other problems with the air wedge are the increasing axial interference of reflections between the layers at very narrow wedge spacings. If the wedge spacing is close to the wavelength of the light source, fringe artefacts increasingly obfuscate the wedge visibility and inhibit the accurate measurement of the axial resolution. Although we could not reliably replicate axial air wedge interference, which appears attenuated due to the broad bandwidth of the light source, it shows that the air wedge is valuable in investigating structural visibility. The air wedge using non-ideal reflecting materials would provide a controlled structure to evaluate different conditions that reduce resolution and visibility in actual samples.

Although, the air-wedge measurement method is limited due to the intensity noise in the image, it is sufficient to obtain a value for the improvement of resolution by direct measurement. However, it also shows that it can provide a rich set of additional information about the visibility an OCT system can provide. Relating to Fig. 9 for instance, the uncertainty of the visibility due to noise is a major indicator of sensitivity performance. The visibility uncertainties for the Telesto III system are narrower overall compared to the described HR-SD-OCT system but has a more consistent spread per segment, indicating that some contrast stretching is performed to obtain optimal image results. In comparison, the described HR-SD-OCT system has a large spread due to the high NA lens, but a very narrow spread per segment, indicating that best sensitivity is obtained at the scan centre.

C. Imaging Results

To demonstrate the imaging performance of the designed HR-SD-OCT system and compare it to the Telesto III system from Thorlabs, we imaged non-biological and biological samples. Fig. 11 shows B-scan images of multilayer Scotch tape using a similar high-NA sample lens in both systems. Although, in both cases, the depth visibility is limited, the speckle noise for the described HR-SD-OCT system is somewhat better. Fig. 12(a) and (b) shows B-scan images obtained from volunteer's fingertip.

The isometry of the image voxel improves the structural visibility for our HR-SD-OCT system compared to the Telesto system. In Fig. 12(a) and (b) the zoomed regions (red boxes) show that for the HR-SD-OCT the speckle washout is reduced, whereas for the Telesto system the contrast is improved.
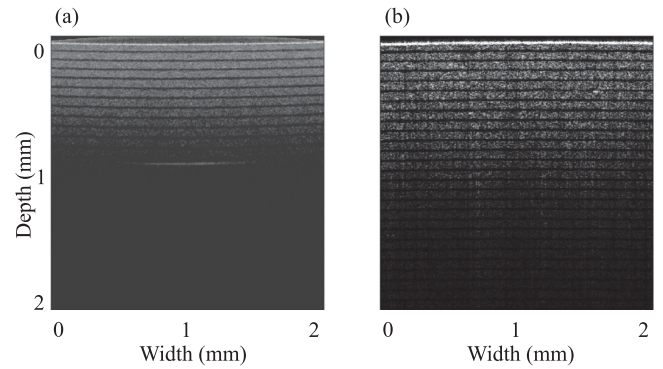

Fig. 11. Comparison of the HR-SD-OCT (a) vs. the Telesto III (b) using Scotch tape. Image (a) shows smoother speckle structure due to the isometric voxel size.

Fig. 12(c) to (f) show images from a green cucumber compared between the described HR-SD-OCT and the Telesto III system. Fig. 12(c) and (d) confirm that the speckle structures improve due to the isometric voxel shape and consequently reveal more structural details. This would confirm the advantages of isometric imaging to produce a better contrast and improved structural visibility. Fig. 12(e) and (f) show en face images from the HR-SD-OCT and Telesto III respectively.

It should be noted that the HR-SD-OCT sacrifices depth visibility due to the high NA sample lens. The lens has the most substantial contribution to reduced depth visibility. Another factor could be the usable spectral resolution of the spectrometer due to a limited spectral illumination. The maximum imaging depth z_{max} for a spectral-domain OCT is described by $z_{max} = \frac{\lambda_c^2}{4n\delta\lambda}$ where λ_c is the centre wavelength, n is the refractive index, and $\delta\lambda$ is the wavelength resolution of the spectrometer [50]. Although our system tries to accommodate a maximal bandwidth, not all camera pixels receive equal intensity. Therefore, the maximum spectrometer resolution achievable is reduced, which in retrospect limits the depth visibility.

According to literature, the local contrast, in conjunction with the spatial frequency of structures, is relevant in determining the ability of an imaging system to capture or reconstruct features of interest [51]. The contrast-to-noise ratio (CNR) is then the ratio of the local contrast to the image noise. Various other literature sources describe the selection of specific regions to obtain a noise level, and it is usually acknowledged that the CNR is not an absolute metric but a relative metric to compare the local contrast of imaging systems. Conventionally, the root-mean-square or the standard deviation of the noise is obtained from a common image region. However, for the images available for this study and the purpose of comparing between the commercial system (Telesto III) and the investigated fibre-based OCT system, we obtain the noise from the median level in the region of interest. Equation (3) describes the mathematical relation to compute the CNR based on the region of interest in the image (I_{ROI}):

$$\text{CNR} = (\max(I_{ROI}) - \min(I_{ROI})) / \text{median}(I_{ROI}) \quad (3)$$

The median value is dominated by the noise level, while larger intensity values from structures have little effect. Consequently,
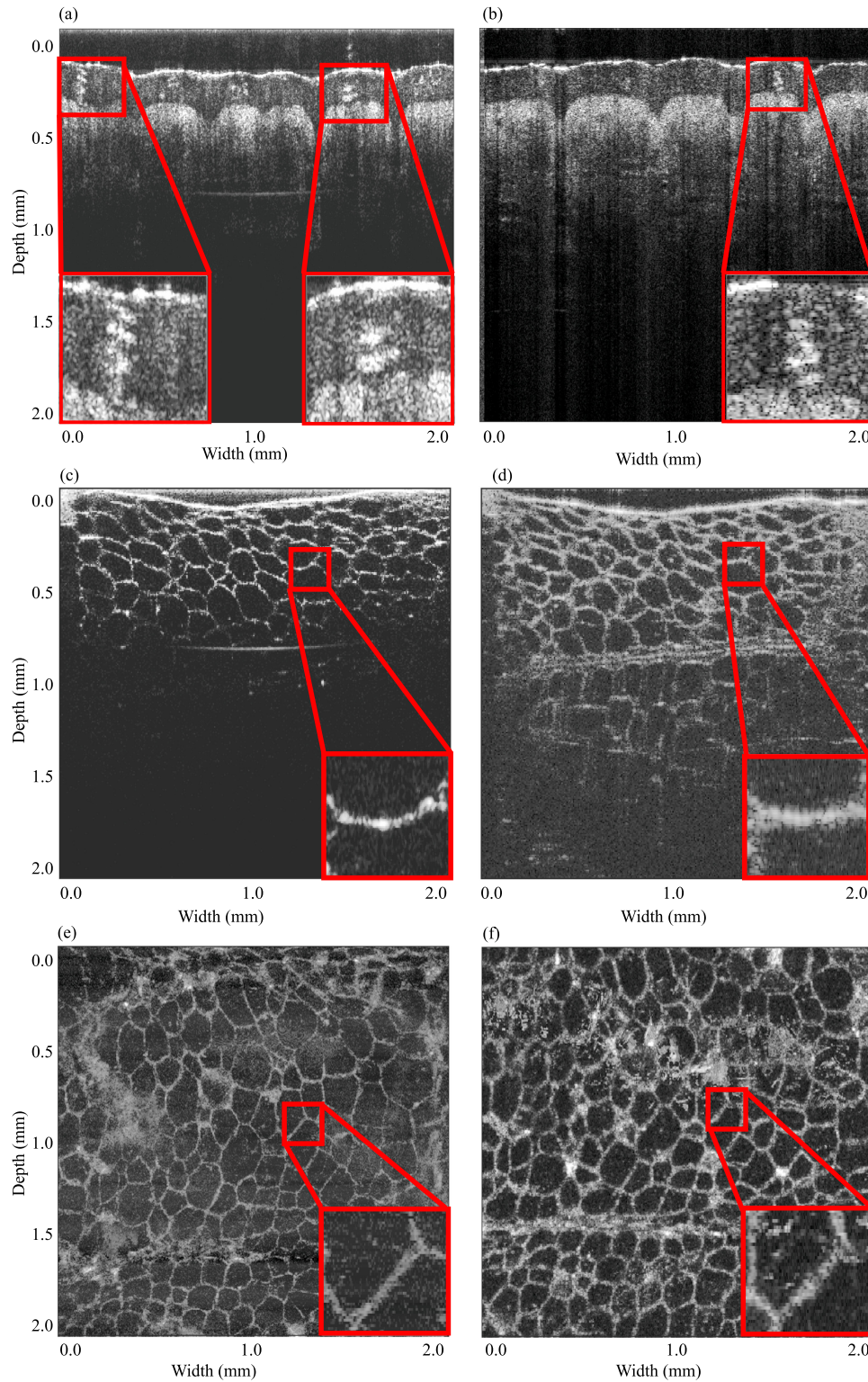
Fig. 12. Comparison of the HR-SD-OCT (left column) vs Telesto III (right column). Images (a) and (b) show a fingertip and the zoomed regions (red box) show a less pronounced speckle washout for the HR-SD-OCT system, which may be attributed to the improved isometric voxel shape using the high-NA sample lens. B-frame images of green cucumber (c) and (d). Red boxes from the same selected region show that again the speckle washout for the HR-SD-OCT system is less pronounced. En face images of green cucumber (e) and (f). The red boxes from the same selected region show a sharper image, which is to be expected due to the higher NA lens used for the HR-SD-OCT vs the Telesto III.

TABLE III
CNR COMPARED BETWEEN TELESTO AND HIGH-RESOLUTION SYSTEM

	Telesto	High-resolution system
Finger tip	0.44	2.44
Cucumber B-frame	1.28	9.00
Cucumber en face	0.69	3.27

we can use the calculated CNR to compare how much local contrast for selected structures in the region of interest is available, as long as the structures are similar in both images and do not fill the whole region of interest (see Fig. 12).

Table III confirms that the investigated high-resolution system has larger CNR values compared to the Telesto system.

Minor differences in the images are expected as it was not possible to equip both systems with the same lens type. Nevertheless, Table III shows a notable increase of CNR values consistently for three different structures for the investigated HR-SD-OCT system.

IV. CONCLUSION

We have designed a fibre-based HR-SD-OCT system and evaluated a simple air-wedge method to compare axial resolution directly. We described low-cost construction of the air-wedges, which should be easily accessible for many laboratories, but also has the potential to work with commercially fabricated wedges. The characterization of the axial resolution with air-wedges provides the opportunity to work with different AR coatings compared to using conventional mirrors. Future developments could also include the use of custom optical mounts that allow direct adjustment of the wedge spacing and slope. Nevertheless, the air-wedge also provides some information of the uncertainty of reproducing a PSF, which may be of interest for high-end image quality quantification.

Moreover, we studied the feasibility of using a broad bandwidth for a fibre-based OCT system in conjunction with a high-NA sample lens to improve the isometric shape of the image voxels. Especially in conjunction with the broad bandwidth light source, we can see strong indicators for improved structural visibility in B-frame and en face images. After quantitative CNR comparison, it is confirmed that high-resolution system improved the structural visibility.

The axial resolution of the HR-SD-OCT was calculated to be 3.7 microns based on the spectral bandwidth at FWHM and was measured with a Gaussian fit on the data recorded from the sample mirror to be 3.8 microns. To the best of our knowledge, this surpasses the best axial resolution of any fibre-based OCT system at 1300 nm centre wavelength reported. The lateral resolution for a scan range of 2 mm was simulated with 6 microns, and the image of the USAF target showed full separation of elements with a spacing of 11 microns. We compared this resolution with a Telesto III system that is specified with 5.5 microns in air.

Consequently, the HR-SD-OCT has about 1.4 times better axial resolution. The air-wedge analysis provided a mean axial resolution of 13 microns for the Telesto and 11 microns for

the HR-SD-OCT, which relates to about 1.2 times better axial resolution. The larger measured values using the air-wedge are plausible, as the light must pass through the glass body from the top. This would also allow future research of how the refractive index affects the axial resolution.

The improved image quality in conjunction to isometric image voxel geometry is of major interest for conventional OCT imaging [52]–[57]. Our ongoing research to apply nano-sensitive OCT can benefit from the extended spectral bandwidth which permits access to a wider distribution of spatial frequencies and can improve the dynamic range, which is the subject of future research.

ACKNOWLEDGMENT

REFERENCES

[1] D. Huang *et al.*, "Optical coherence tomography," *Science*, vol. 254, no. 5035, pp. 1178–1181, Nov. 1991.

[2] J. Schmitt, "Optical coherence tomography (OCT): A review," *IEEE J. Sel. Topics Quantum Electron.*, vol. 5, no. 4, pp. 1205–1215, Jul./Aug. 1999.

[3] A. C. Akcay, K. S. Lee, L. R. Furenlid, M. A. Costa, and J. P. Rolland, "Compact low-cost detection electronics for optical coherence imaging," *Opt. Eng.*, vol. 45, no. 7, Jul. 2006, Art. no. 070504.

[4] M. Mujat *et al.*, "Retinal nerve fiber layer thickness map determined from optical coherence tomography images," *Opt. Exp.*, vol. 13, no. 23, pp. 9480–9491, Nov. 2005.

[5] B. E. Bouma and G. J. Tearney, "Clinical imaging with optical coherence tomography," *Academic Radiol.*, vol. 9, no. 8, pp. 942–953, Aug. 2002.

[6] X. Yao, Y. Gan, C. C. Marboe, and C. P. Hendon, "Myocardial imaging using ultrahigh-resolution spectral domain optical coherence tomography," *J. Biomed. Opt.*, vol. 21, no. 6, Mar. 2016, Art. no. 0 61006.

[7] J. G. Fujimoto, S. A. Boppart, G. J. Tearney, B. E. Bouma, C. Pitris, and M. E. Brezinski, "High resolution in vivo intra-arterial imaging with optical coherence tomography," *Heart*, vol. 82, no. 2, pp. 128–133, Aug. 1999.

[8] G. J. Tearney *et al.*, "Quantification of macrophage content in atherosclerotic plaques by optical coherence tomography," *Circulation*, vol. 107, no. 1, pp. 113–119, Jan. 2003.

[9] S. A. Boppart, W. Luo, D. L. Marks, and K. W. Singletary, "Optical coherence tomography: Feasibility for basic research and image-guided surgery of breast cancer," *Breast Cancer Res. Treat.*, vol. 84, no. 2, pp. 85–97, Mar. 2004.

[10] A. F. Zuluaga, M. Follen, I. Boiko, A. Malpica, and R. Richards-Kortum, "Optical coherence tomography: A pilot study of a new imaging technique for noninvasive examination of cervical tissue," *Amer. J. Obstet. Gynecol.*, vol. 193, no. 1, pp. 83–88, Jul. 2005.

[11] B. W. Colston, M. J. Everett, L. B. D. Silva, L. L. Otis, P. Stroeve, and H. Nathel, "Imaging of hard- and soft-tissue structure in the oral cavity by optical coherence tomography," *Appl. Opt.*, vol. 37, no. 16, pp. 3582–3585, Jun. 1998.

[12] L. L. Otis, B. W. Colston, M. J. Everett, and H. Nathel, "Dental optical coherence tomography: A comparison of two in vitro systems," *Dento Maxillo Facial Radiol.*, vol. 29, no. 2, pp. 85–89, Mar. 2000.

[13] A. Z. Freitas, D. M. Zezell, N. D. Vieira, A. C. Ribeiro, and A. S. L. Gomes, "Imaging carious human dental tissue with optical coherence tomography," *J. Appl. Phys.*, vol. 99, no. 2, Jan. 2006, Art. no. 024906.

[14] J. Olsen, J. Holmes, and G. B. E. Jemec, "Advances in optical coherence tomography in dermatology—A review," *J. Biomed. Opt.*, vol. 23, no. 4, Apr. 2018, Art. no. 040901.

[15] N. M. Israelsen *et al.*, "The value of ultrahigh resolution OCT in dermatology–delineating the dermo-epidermal junction, capillaries in the dermal papillae and vellus hairs," *Biomed. Opt. Exp.*, vol. 9, no. 5, pp. 2240–2265, May 2018.

[16] R. Steiner, K. Kunzi-Rapp, and K. Scharffetter-Kochanek, "Optical coherence tomography: Clinical applications in dermatology," *Med. Laser Appl.*, vol. 18, no. 3, pp. 249–259, Jan. 2003.

[17] A. M. Zysk, F. T. Nguyen, A. L. Oldenburg, S. A. Boppart, and D. L. Marks, "Optical coherence tomography: A review of clinical development from bench to bedside," *J. Biomed. Opt.*, vol. 12, no. 5, pp. 051 403–051403-21, 2007.

[18] M. F. Shirazi, M. Jeon, and J. Kim, "Structural analysis of polymer composites using spectral domain optical coherence tomography," *Sensors*, vol. 17, no. 5, pp. 1155–1166, May 2017.

[19] P. Meemon *et al.*, "Optical coherence tomography enabling non destructive metrology of layered polymeric GRIN material," *Sci. Rep.*, vol. 3, no. 1, pp. 1709–1719, Apr. 2013.

[20] K. M. Kennedy, S. Es'haghian, L. Chin, R. A. McLaughlin, D. D. Sampson, and B. F. Kennedy, "Optical palpation: Optical coherence tomography-based tactile imaging using a compliant sensor," *Opt. Lett.*, vol. 39, no. 10, pp. 3014–3017, May 2014.

[21] D. Culemann, A. Knuettel, and E. Voges, "Integrated optical sensor in glass for optical coherence tomography (OCT)," *IEEE J. Sel. Topics Quantum Electron.*, vol. 6, no. 5, pp. 730–734, Sep./Oct. 2000.

[22] J. F. de Boer, B. Cense, B. H. Park, M. C. Pierce, G. J. Tearney, and B. E. Bouma, "Improved signal-to-noise ratio in spectral-domain compared with time-domain optical coherence tomography," *Opt. Lett.*, vol. 28, no. 21, pp. 2067–2069, Nov. 2003.

[23] M. Wojtkowski, T. Bajraszewski, P. Targowski, and A. Kowalczyk, "Real-time in vivo imaging by high-speed spectral optical coherence tomography," *Opt. Lett.*, vol. 28, no. 19, pp. 1745–1747, Oct. 2003.

[24] R. Leitgeb, C. K. Hitzenberger, and A. F. Fercher, "Performance of Fourier domain vs. time domain optical coherence tomography," *Opt. Exp.*, vol. 11, no. 8, pp. 889–894, Apr. 2003.

[25] M. Choma, M. Sarunic, C. Yang, and J. Izatt, "Sensitivity advantage of swept source and Fourier domain optical coherence tomography," *Opt. Exp.*, vol. 11, no. 18, pp. 2183–2189, Sep. 2003.

[26] M. Wojtkowski, V. J. Srinivasan, T. H. Ko, J. G. Fujimoto, A. Kowalczyk, and J. S. Duker, "Ultrahigh-resolution, high-speed, Fourier domain optical coherence tomography and methods for dispersion compensation," *Opt. Exp.*, vol. 12, no. 11, pp. 2404–2422, May 2004.

[27] G. Humbert *et al.*, "Supercontinuum generation system for optical coherence tomography based on tapered photonic crystal fibre," *Opt. Exp.*, vol. 14, no. 4, pp. 1596–1603, Feb. 2006.

[28] M. Szkulmowski *et al.*, "Quality improvement for high resolution in vivo images by spectral domain optical coherence tomography with supercontinuum source," *Opt. Commun.*, vol. 246, no. 4, pp. 569–578, Feb. 2005.

[29] P. Cimalla, J. Walther, M. Mehner, M. Cuevas, and E. Koch, "Simultaneous dual-band optical coherence tomography in the spectral domain for high resolution in vivo imaging," *Opt. Exp.*, vol. 17, no. 22, pp. 19486–19500, Oct. 2009.

[30] J. Barrick, A. Doblas, M. R. Gardner, P. R. Sears, L. E. Ostrowski, and A. L. Oldenburg, "High-speed and high-sensitivity parallel spectral-domain optical coherence tomography using a supercontinuum light source," *Opt. Lett.*, vol. 41, no. 24, pp. 5620–5623, Dec. 2016.

[31] Y.-J. You, C. Wang, Y.-L. Lin, A. Zaytsev, P. Xue, and C.-L. Pan, "Ultrahigh-resolution optical coherence tomography at 1.3 μm central wavelength by using a supercontinuum source pumped by noise-like pulses," *Laser Phys. Lett.*, vol. 13, no. 2, Dec. 2015, Art. no. 025101.

[32] C. Chen, W. Shi, R. Reyes, and V. X. D. Yang, "Buffer-averaging supercontinuum source based spectral domain optical coherence tomography for high speed imaging," *Biomed. Opt. Exp.*, vol. 9, no. 12, pp. 6529–6544, Dec. 2018.

[33] M. Maria *et al.*, "A comparative study of noise in supercontinuum light sources for ultra-high resolution optical coherence tomography," *Proc. SPIE*, vol. 10056, Mar. 2017, Art. no. 1005600.

[34] K. C. Zhou, R. Qian, S. Degan, S. Farsiu, and J. A. Izatt, "Optical coherence refraction tomography," *Nature Photon.*, vol. 13, no. 11, pp. 794–802, Nov. 2019.

[35] K. C. Zhou, R. Qian, S. Farsiu, and J. A. Izatt, "Spectroscopic optical coherence refraction tomography," *Opt. Lett.*, vol. 45, no. 7, pp. 2091–2094, Apr. 2020.

[36] C.-K. Chang *et al.*, "Segmentation of nucleus and cytoplasm of a single cell in three-dimensional tomogram using optical coherence tomography," *J. Biomed. Opt.*, vol. 22, no. 3, Mar. 2017, Art. no. 036003.

[37] K. Q. Kieu, N. N. Peyghambarian, J. Klein, J. K. Barton, and A. Evans, "Ultrahigh resolution all-reflective optical coherence tomography system with a compact fiber-based supercontinuum source," *J. Biomed. Opt.*, vol. 16, no. 10, Oct. 2011, Art. no. 106004.

[38] S. Ishida and N. Nishizawa, "Quantitative comparison of contrast and imaging depth of ultrahigh-resolution optical coherence tomography images in 800 nm wavelength region," *Biomed. Opt. Exp.*, vol. 3, no. 2, pp. 282–294, Jan. 2012.

[39] Y. Lu *et al.*, "Non-planar calibration phantoms for optical coherence tomography," in *Proc. SPIE*, vol. 10544, Feb. 2018, pp. 148–154.

[40] S. Braun, "Windows," in *Encyclopedia of Vibration*, S. Braun, Ed. Oxford, U.K.:Elsevier, Jan. 2001, pp. 1587–1595.

[41] J. G. Robertson, "Quantifying resolving power in astronomical spectra," *Pub. Astronomical Soc. Aust.*, vol. 30, 2013, Art. no. e048.

[42] T. Latychevskaia, "Lateral and axial resolution criteria in incoherent and coherent optics and holography, near- and far-field regimes," *Appl. Opt.*, vol. 58, no. 13, pp. 3597–3603, May 2019.

[43] S. V. Aert, D. V. Dyck, and A. J. den Dekker, "Resolution of coherent and incoherent imaging systems reconsidered - Classical criteria and a statistical alternative," *Opt. Exp.*, vol. 14, no. 9, pp. 3830–3839, May 2006.

[44] R. S. Kallweit and L. C. Wood, "The limits of resolution of zero-phase wavelets," *Geophysics*, vol. 47, no. 7, pp. 1035–1046, Jul. 1982.

[45] R. Barakat, "Application of apodization to increase two-point resolution by the Sparrow criterion I. Coherent illumination," *J. Opt. Soc. Amer.*, vol. 52, no. 3, pp. 276–283, Mar. 1962.

[46] M. Moskovits, "Criterion for determining resolving power in the optical near field," *J. Nanophotonics*, vol. 11, no. 4, Dec. 2017, Art. no. 046018.

[47] S. Van der Walt *et al.*, "Scikit-image: Image processing in Python," *PeerJ*, vol. 2, Jun. 2014, Art. no. e453.

[48] M. Newville *et al.*, lmfit/lmfit-py: 1.0.3. Zenodo, 2021, doi: 10.5281/zenodo.5570790.

[49] X. Liu, S. Chen, D. Cui, X. Yu, and L. Liu, "Spectral estimation optical coherence tomography for axial super-resolution," *Opt. Exp.*, vol. 23, no. 20, pp. 26521–26532, Oct. 2015.

[50] B. Akca *et al.*, "Toward spectral-domain optical coherence tomography on a chip," *IEEE J. Sel. Topics Quantum Electron.*, vol. 18, no. 3, pp. 1223–1233, May/Jun. 2012.

[51] E. Peli, "Contrast in complex images," *J. Opt. Soc. Amer. A*, vol. 7, no. 10, pp. 2032–2040, Oct. 1990.

[52] S. A. Alexandrov, H. M. Subhash, A. Zam, and M. Leahy, "Nano-sensitive optical coherence tomography," *Nanoscale*, vol. 6, no. 7, pp. 3545–3549, Mar. 2014.

[53] S. Alexandrov *et al.*, "Spatial frequency domain correlation mapping optical coherence tomography for nanoscale structural characterization," *Appl. Phys. Lett.*, vol. 115, no. 12, Sep. 2019, Art. no. 121105.

[54] Y. Zhou, S. Alexandrov, A. Nolan, N. Das, R. Dey, and M. Leahy, "Noninvasive detection of nanoscale structural changes in cornea associated with cross-linking treatment," *J. Biophotonics*, vol. 13, no. 6, 2020, Art. no. e201960234.

[55] C. Lal, S. Alexandrov, S. Rani, Y. Zhou, T. Ritter, and M. Leahy, "Nanosensitive optical coherence tomography to assess wound healing within the cornea," *Biomed. Opt. Exp.*, vol. 11, no. 7, pp. 3407–3422, Jul. 2020.

[56] N. Das, S. Alexandrov, Y. Zhou, K. E. Gilligan, R. M. Dwyer, and M. Leahy, "Nanoscale structure detection and monitoring of tumour growth with optical coherence tomography," *Nanoscale Adv.*, vol. 2, no. 7, pp. 2853–2858, May 2020.

[57] S. Alexandrov *et al.*, "Accessing depth-resolved high spatial frequency content from the optical coherence tomography signal," *Sci. Rep.*, vol. 11, no. 1, Aug. 2021, Art. no. 17123.